Available online at www.sciencedirect.com

Journal of the European Ceramic Society 28 (2008) 2545–2555

www.elsevier.com/locate/jeurceramsoc

$\{10\bar{1}1\}$ artificial epitaxy of ZnO on glass via pulse laser deposition

Bang-Hao Huang[a], Pouyan Shen[a], Shuei-Yuan Chen[b,*]

[a] *Institute of Materials Science and Engineering, Department of Materials and Optoelectronic Science,*
National Sun Yat-Sen University, Kaohsiung, Taiwan, ROC
[b] *Department of Mechanical Engineering, I-Shou University, Kaohsiung, Taiwan, ROC*

Received 14 December 2007; received in revised form 9 March 2008; accepted 15 March 2008
Available online 29 April 2008

Abstract

Wurtzite (W)-type ZnO condensates showed preferred orientation $\{10\bar{1}1\}$ when deposited on glass substrate by pulse laser ablation on Zn target in the presence of oxygen. Such an artificial epitaxy depends on the well-developed $\{10\bar{1}1\}$ surfaces of the condensates, which enabled $\{10\bar{1}1\}$-specific coalescence to form twin and single crystal regardless of the co-deposited Zn. The W-ZnO condensates have decreasing particle size with increasing oxygen flow rate and a considerable residual stress due to the combined effects of rapid heating/cooling and thermal/lattice mismatch with Zn following parallel epitaxy or $(01\bar{1}\bar{1})_{\text{W-ZnO}}//(01\bar{1}0)_{\text{Zn}}$; $[\bar{1}2\bar{1}3]_{\text{W-ZnO}}//[0001]_{\text{Zn}}$ involving $\{10\bar{1}1\}$ slip.

Keywords: Artificial epitaxy; ZnO; Condensate shape; Glass substrate; TEM

1. Introduction

Zinc oxide of wurtzite-type structure, an important semiconducting and piezoelectric material, can be tailored as various novel nanostructures by thermal evaporation because of its polar surfaces, which have nontransferable ionic charges arranged in such a configuration to minimize the electrostatic energy.[1] The polar surfaces are usually $\pm(0001)$, but occasionally $\pm\{0\bar{1}11\}$ as observed in a nanohelical structure of W-ZnO.[2] According to recent high-resolution TEM and simulation,[3] the oxygen-terminated $(000\bar{1})$ polar surface is flat, whereas Zn-terminated (0001) polar surface appears to have Zn vacancies and outward displacement of Zn ions. The oxygen-terminated $(0\bar{1}11)$ polar surface has two groups of oxygen ion positions; whereas Zn-terminated $(01\bar{1}\bar{1})$ polar surface was not observed presumably due to its higher surface energy.[3]

The polar (0001) surfaces and preferred orientation of W-ZnO are well developed when epitaxially deposited on specific surface of crystalline substrates such as $(2\bar{1}\bar{1}0)$ sapphire,[4] and $(010)/(100)$-facetted tetragonal Sn particles.[5] It is not known to have W-ZnO $\{10\bar{1}1\}$ preferred orientation on any substrate until the present study via a very energetic pulsed laser ablation condensation of the W-ZnO. The cause of this unusual preferred orientation is clarified to be the shape of the nanocondensates, which justifies a $\{10\bar{1}1\}$-specific coalescence process during laser ablation condensation. This type of preferred orientation is analogous to so-called artificial epitaxy (graphoepitaxy) on amorphous substrate with crystallographically arranged microrelief striations.[6] The $\{10\bar{1}1\}$-faceted condensates are also crucial to the fabrication of rod-like W-ZnO whiskers with unusual habit, i.e. extending along the zone axes of the well-developed polar surfaces $\{10\bar{1}1\}$.[7]

2. Experimental

The Zn target with negligible impurities (99.9% pure) was subject to energetic Nd-YAG-laser (Lotis, 1064 nm in wavelength, beam mode: TEM00) pulse irradiation in air or in a chamber vacuumed down to 4×10^{-3} Pa, with a specified oxygen flow rate from 0 to 30 mL/min. Laser beam was focused to a spot size of 0.03 mm^2 on the target under laser pulse energy of 560 mJ/pulse, i.e. power density of 1.17×10^{12} W/cm^2 given pulse time duration of 16 ns at 10 Hz under Q-switch mode. Soda-lime glass or copper grids overlaid with a carbon-coated collodion film without a preheating treatment were fixed in position by a holder at a distance of 2.5–10 mm from the target to collect the Zn/ZnO condensates. Additional experiment under

---

* Corresponding author.
E-mail address: steven@isu.edu.tw (S.-Y. Chen).

0955-2219/$ – see front matter © 2008 Elsevier Ltd. All rights reserved.
doi:10.1016/j.jeurceramsoc.2008.03.012

Table 1
Pulsed Nd-YAG laser ablation conditions for the preparation of the Zn/W-ZnO deposits on soda-lime glass

Sample #	Laser mode	Pulsed energy (mJ/pulse)	Flow rate of specified gas	Deposition time (min)
Vac-0	Q-switch	560	In vacuum without gas purge	10
Vac-10	Q-switch	560	In vacuum under 10 mL/min O_2	15
Vac-20	Q-switch	560	In vacuum under 20 mL/min O_2	15
Vac-30	Q-switch	560	In vacuum under 30 mL/min O_2	15
Air-0	Free-run	1040	In air under 50 L/min O_2	10

free run mode at much higher pulse energy of 1040 mJ/pulse and a three orders-of-magnitude higher oxygen flow rate of 50 L/min in air was conducted for a comparison of preferred orientation and shape of the condensates. The laser parameters, deposition time and oxygen flow rate for all samples are compiled in Table 1.

The oxygen flow rate dependence of the size, orientation and lattice parameters of the Zn and ZnO phases in the samples deposited on glass was determined by X-ray diffraction (XRD, Cu Kα, D5000 instrument). High-resolution XRD (Cu Kα, D1 instrument) step-scan with 0.001° increment was also employed to resolve the nearly superimposed $\{1\,0\,\bar{1}\,1\}_{\text{W-ZnO}}$ and $(0\,0\,0\,2)_{\text{Zn}}$ peaks. Optical microscopy under plane polarized light and scanning electron microscopy (SEM, JEOL6330, 10 kV) were used to study the size distribution and microstructures, in particular the extent of coalescence of the condensates that accounts for the preferred orientation of the deposits on glass. The composition and crystal structures of the individual condensates on the carbon-coated collodion film were characterized by field emission transmission electron microscopy (TEM, FEI Tecnai G2 F20 at 200 kV) coupled with selected area electron diffraction (SAED), and point-count energy dispersive X-ray (EDX) analysis at a beam size of 5 nm. The EDX analysis was performed using K shell counts for Zn and O, and the principle of ratio method without absorption correction.[8]

3. Results

The deposits showed fair translucency under naked eye when prepared under specified oxygen flow rates. This is in drastic contrast with the case of opaque coating on glass prepared in vacuum without oxygen flow. In general, the plumes are bluish regardless of oxygen flow rate. However, the phase identity and microstructures were affected by oxygen flow rate as addressed in the following.

3.1. Preferred orientation of the deposit on glass according to XRD

The XRD whole trace showed a strong preferred orientation of $(0\,0\,0\,1)_{\text{Zn}}$ and $\{1\,0\,\bar{1}\,1\}_{\text{W-ZnO}}$ for all the condensates

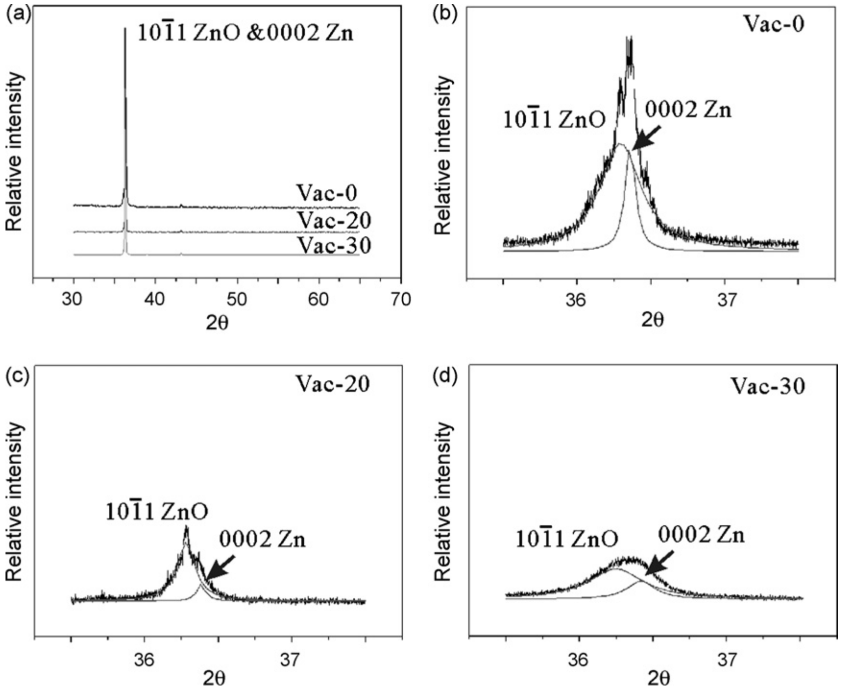

Fig. 1. (a) XRD (Cu Kα) traces of the deposit on soda-lime glass prepared by pulsed laser ablation on Zn target at 560 mJ/pulse in vacuum under specified oxygen flow rate 0, 20 and 30 mL/min. The preferred $(0\,0\,0\,1)_{\text{Zn}}$ and $(1\,0\,\bar{1}\,1)_{\text{W-ZnO}}$ co-orientation was confirmed by high-resolution XRD (Cu Kα) step-scan trace and Lorenz curve fitting showing well resolved $(1\,0\,\bar{1}\,1)_{\text{W-ZnO}}$ and $(0\,0\,0\,2)_{\text{Zn}}$ peaks for the case of 0, 20 and 30 mL/min in (b), (c) and (d), respectively. The small peak at about 43° in (a) is the $(1\,0\,\bar{1}\,1)$ reflection of zinc.

deposited on soda-lime glass at 560 mJ/pulse and 0–30 mL/min oxygen flow rate in vacuum (Fig. 1). The corresponding high-resolution XRD step-scan showed well resolved $\{1\,0\,\bar{1}\,1\}_{\text{W-ZnO}}$ and $(0\,0\,0\,2)_{\text{Zn}}$ peaks with varied relative intensity and d-spacing as a function of oxygen flow rate (Fig. 1). Our additional experiment of laser ablation condensation at a relatively high pulse energy of 1040 mJ/pulse and a high oxygen flow rate of 50 L/min in air showed also the preferred orientations $(0\,0\,0\,1)_{\text{Zn}}$ and $\{1\,0\,\bar{1}\,1\}_{\text{W-ZnO}}$ for the deposit on glass substrate (not shown). The preferred orientations of the W-ZnO and Zn deposits were independently developed because $(0\,0\,0\,1)_{\text{Zn}}$ is not parallel to $\{1\,0\,\bar{1}\,1\}_{\text{W-ZnO}}$ given the epitaxial relationships of the condensates determined by TEM.

3.2. Size and coalescence behavior of the deposits on glass by optical polarized microscopy and SEM

Optical polarized microscopic observations of the deposit overlaid on glass in vacuum showed opaque Zn, birefringent W-ZnO, and craters ca. 40 μm in diameter presumably due to impact of Zn-rich plumes. The tiny W-ZnO condensates were significantly assembled at 20 mL/min of oxygen and coalesced up to tens of micrometers in size at 30 mL/min of oxygen. The coalesced W-ZnO condensates showed interference color rather than isotropic extinction under crossed polarizers. This is in accord with the preferred orientation $(1\,0\,\bar{1}\,1)$ rather than $(0\,0\,0\,1)$, the latter would otherwise be extinct under crossed polarizers. The faceted domains with different interference color across planar boundaries (not shown) can be attributed to $\{1\,0\,\bar{1}\,1\}$-specific coalescence twinning as manifested by TEM observations of the condensates collected on carbon-coated collodion film. Based on the interference color change under an accessory λ retardation plate, the coalesced/elongated W-ZnO condensates were found to have a lower refractive index for the long axis than the short axis. This indicates that the W-ZnO condensates do not coalesce/extend along the crystallographic *c*-axis, i.e. the crystal direction with the greatest refractive index ($n_e = 2.005$).[9]

SEM secondary electron images of the sample deposited on glass in vacuum showed more clearly the shape of the plume-induced craters and the size distribution of the condensates (Fig. 2a). The image magnified from the relatively flat area showed individual W-ZnO condensates less than 0.3 μm in size, which have well-developed facets and were more or less coalesced. The W-ZnO condensates were finer in size (0.1–0.05 μm) yet significantly sintered when deposited under a

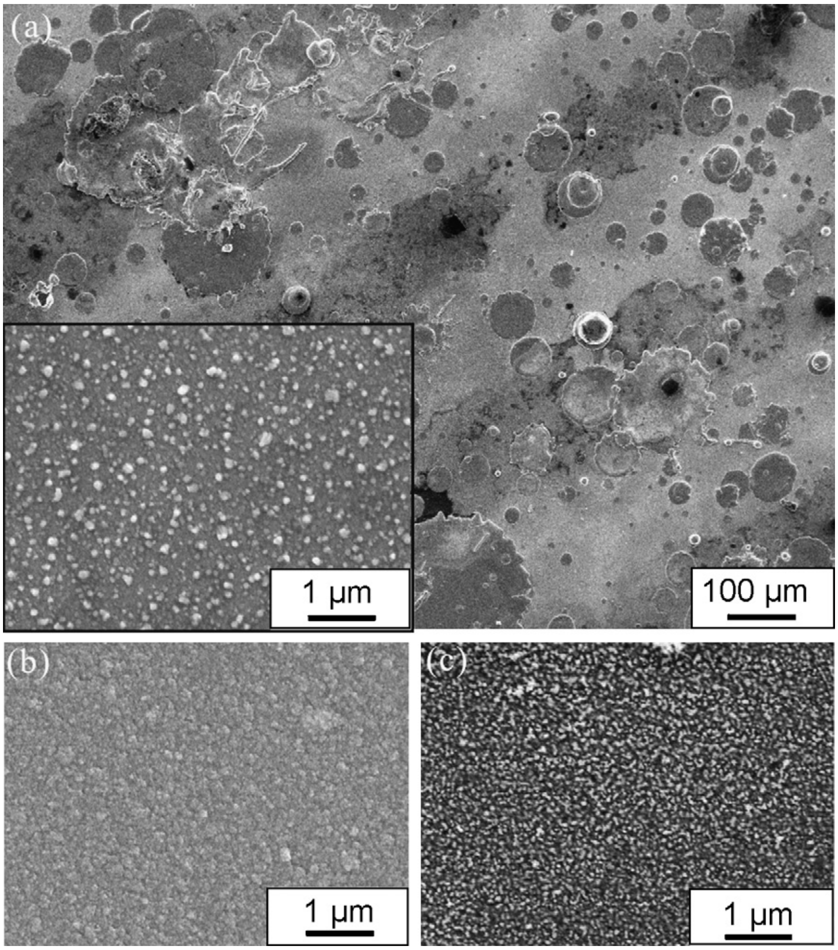

Fig. 2. SEM secondary electron images showing the top-view of the deposit on glass prepared by pulsed laser ablation on Zn target at 560 mJ/pulse under oxygen flow rate of (a) 0 mL/min, (b) 20 mL/min, and (c) 30 mL/min in vacuum. The inset of (a) was magnified from area away the tens-of-micron sized craters to show the fine condensates. The condensates are progressively finer in size at a higher oxygen flow rate in (b) and (c).

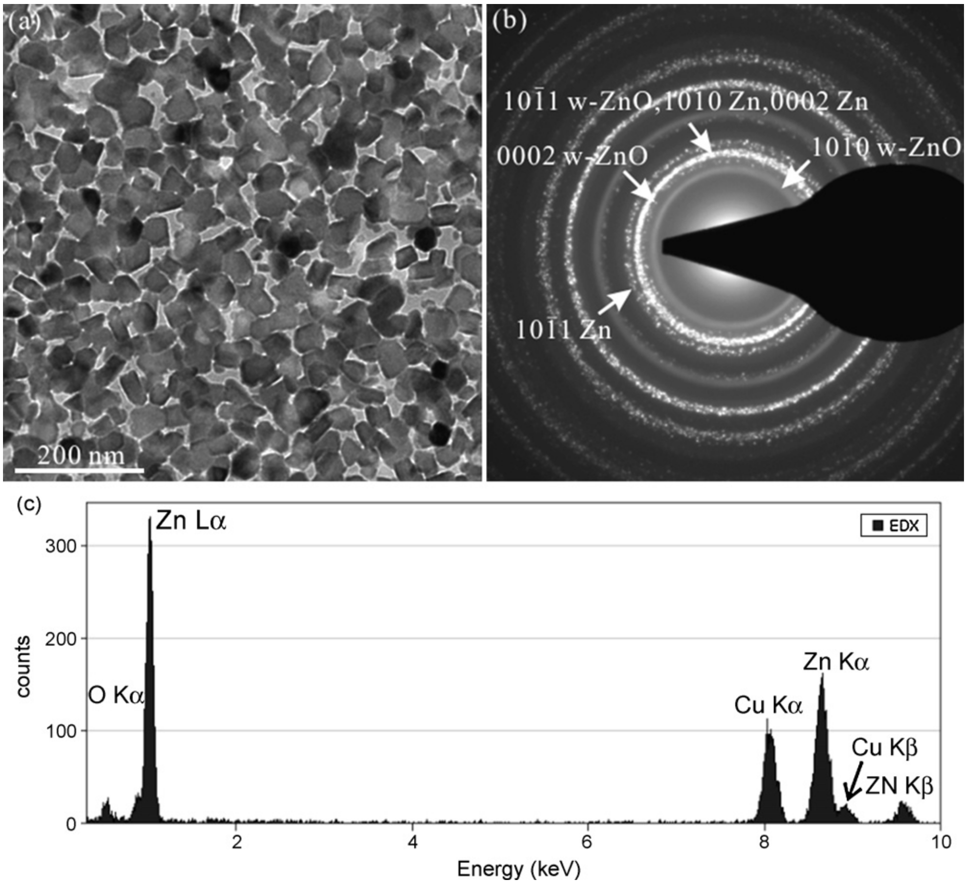

Fig. 3. TEM (a) bright field image and (b) ring SAED pattern of faceted Zn/ZnO condensates, which are ca. 50 nm in size and agglomerated as a close packed manner. (c) EDX spectrum of the Zn/ZnO particle showing strong Zn and O peaks, with Cu peaks from supporting Cu ring. These condensates were produced by pulsed laser ablation on Zn target at 560 mJ/pulse in vacuum and collected on a carbon-coated collodion film.

higher oxygen flow rate of 20 mL/min (Fig. 2b) and 30 mL/min (Fig. 2c) in vacuum, respectively. The thickness of the deposit on glass depends on deposition time (Table 1) and is ca. 20–25 μm on the average based on the birefringence and interference color of the coalesced W-ZnO particles as observed by optical polarized microscopy.

3.3. TEM observations of the condensates collected on carbon-coated collodion film

The representative Zn/W-ZnO condensates collected on the carbon-coated collodion film by laser ablation in vacuum are ca. 50 nm in size with well-developed facets, which were agglomerated as a close packed manner (Fig. 3a) in random orientation as indicated by ring SAED pattern (Fig. 3b). No impurities were detected in the particles using EDX (Fig. 3c).

The finer sized Zn/W-ZnO nanocondensates produced in vacuum under additional 10 mL/min oxygen flow rate for 10 min were significantly solid-state sintered to form a triple junction (Fig. 4a). The Moiré fringes in Fig. 4a are due to intimate intergrowth and overlapping of the Zn/W-ZnO platelets, which affect the thickness and shape of the faceted particle. Still, two-dimensional Fourier transform (Fig. 4b) and schematic indexing (Fig. 4c) were able to show parallel–epitaxial relationship and double diffraction of the overlapped phases in [0 0 0 1] zone axis for some areas of the sample. The inverse Fourier transform (Fig. 4d) showed dislocations and modulated distribution of defect clusters as also evident in the pattern of Moiré fringes. TEM lattice image of a representative nanocondensate with intimate mixture of Zn/W-ZnO in the same specimen showed combined shape and phase changes, in particular with progressively stronger diffractions of Zn phase upon electron irradiation for 1 min (Fig. 5a), 15 min (Fig. 5b) and 30 min (Fig. 5c). (Such changes were also observed for the specimen produced by laser ablation in vacuum without oxygen flow (not shown).) The gradual orientation and crystallographic relationship changes were also manifested by the change of Moiré fringes from Fig. 5a to c. In fact, during this time period, the crystallographic relationship changed from $[0001]_{\text{W-ZnO}}//[0001]_{\text{Zn}}$; $(10\bar{1}0)_{\text{W-ZnO}}//(10\bar{1}0)_{\text{Zn}}$ to $[\bar{1}2\bar{1}3]_{\text{W-ZnO}}//[0001]_{\text{Zn}}$; $(01\bar{1}\bar{1})_{\text{W-ZnO}}//(01\bar{1}0)_{\text{Zn}}$ (Fig. 5b) and the Zn content appeared to increase at the expense of W-ZnO as indicated by the diffraction intensity change (Fig. 5c). The corresponding two-dimensional inverse Fourier transform showed faults/slips parallel to the well-developed $\{01\bar{1}\bar{1}\}_{\text{W-ZnO}}$ as well as $(01\bar{1}0)_{\text{Zn}}$, and $\{\bar{1}100\}_{\text{Zn}}$ (Fig. 5d) despite the interference of the Moiré fringes. This indicates that the $\{10\bar{1}1\}_{\text{W}}$ slip and possibly the

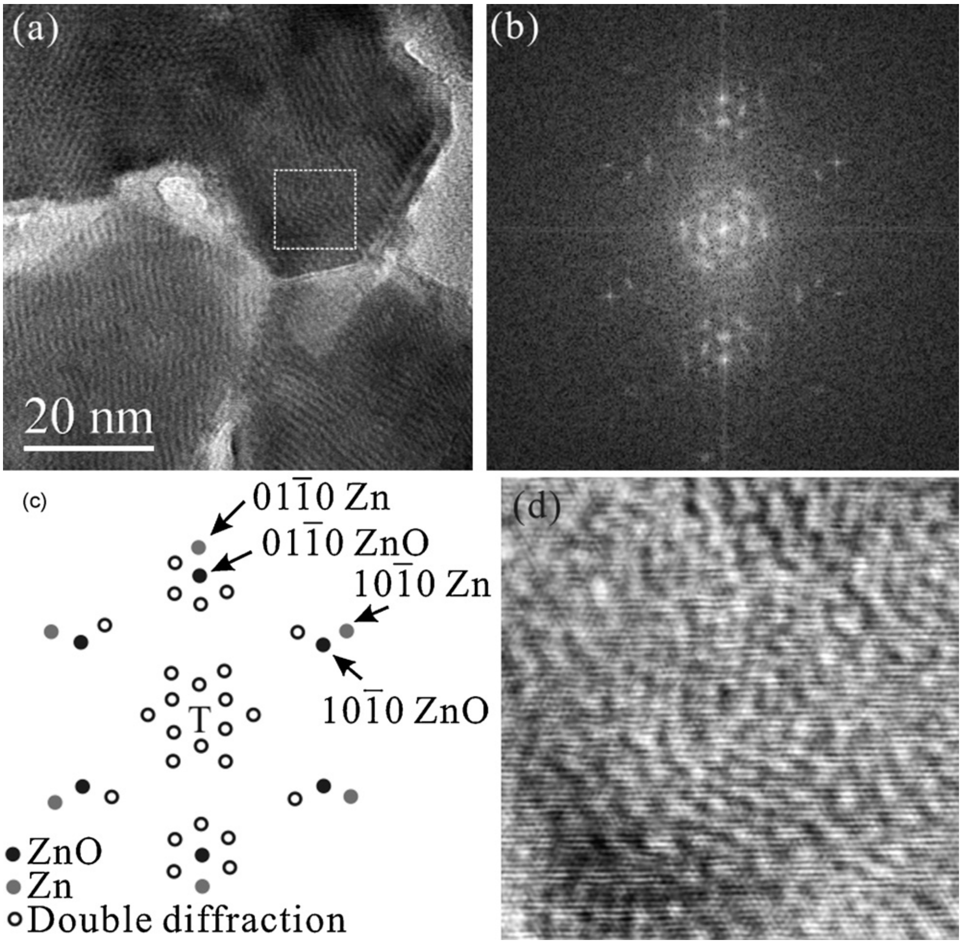

Fig. 4. (a) Lattice image of the Zn/W-ZnO nanocondensates more or less coalesced/sintered to form 120° triple junction, (b) two-dimensional Fourier transform of the square region in (a), (c) schematic indexing showing parallel–epitaxial relationship and double diffraction of the overlapped Zn/W-ZnO in [0 0 0 1] zone axis and (d) inverse Fourier transform of (b) showing dislocations and modulated distribution of defect clusters. Sample produced at 560 mJ/pulse in vacuum under 10 mL/min oxygen flow rate for 10 min.

corresponding Zn slip were involved in such an orientation change.

As for laser ablation conducted in vacuum under oxygen flow rate of 30 mL/min, only W-ZnO nanocondensates were collected on the TEM sample foil (Fig. 6), although Zn particulates were deposited on the glass substrate according to optical microscopic observation (not shown). The ZnO condensates are ca. 5–10 nm in size and agglomerated as nanoparticles chain aggregate (NCA) or in a close packed manner (Fig. 6a) in random orientation as indicated by ring SAED pattern (Fig. 6b). Point-count EDX spectrum of the condensates (Fig. 6c) showed strong Zn and O peaks, with negligible impurities. A higher Zn/O count ratio than reagent grade ZnO powder standard (not shown) indicated it could be a nonstoichiometric $Zn_{1+x}O$ phase. Lattice image (Fig. 7a) coupled with 2D forward (Fig. 7b) and inverse Fourier transform (Fig. 7c) showed well-developed $(0\,1\,\bar{1}\,1)$ and $\{0\,0\,0\,1\}$ polar surfaces for such a nanocondensate.

At a relatively high pulse energy of 1040 mJ/pulse and a high oxygen flow rate of 50 L/min in air, only W-ZnO nanocondensates were collected on TEM sample foil (Fig. 8), although Zn particulates were deposited on the glass substrate according to optical microscopic observation (not shown). The W-ZnO nanocondensates tended to form twinned bicrystals having $(\bar{1}\,1\,0\,1)$ twin boundary as indicated by lattice image in $[2\,\bar{1}\,\bar{1}\,3]$ zone axis in Fig. 8a. Such twinned bicrystals show birefringence difference across the twin boundary under optical polarized microscopy as observed for other samples. There are abundant dislocations with half plane parallel to $(\bar{1}\,1\,0\,1)$ and $(\bar{1}\,0\,1\,1)$ polar surfaces in the twinned bicrystals as indicated by 2D forward (Fig. 8b) and inverse (Fig. 8c) Fourier transform.

4. Discussion

4.1. Oxygen flow rate dependence of size, phase and considerable residual stress of the condensates

A higher oxygen flow rate would decrease the mean free path of the Zn clusters and increase the probability of collision with oxygen to form relatively inert ZnO condensates. As a consequence, there is a progressively finer particle size and decreasing Zn/O atomic ratio (from 4.743 to 1.411, cf. Table 2) for the deposit formed at a higher oxygen flow rate.

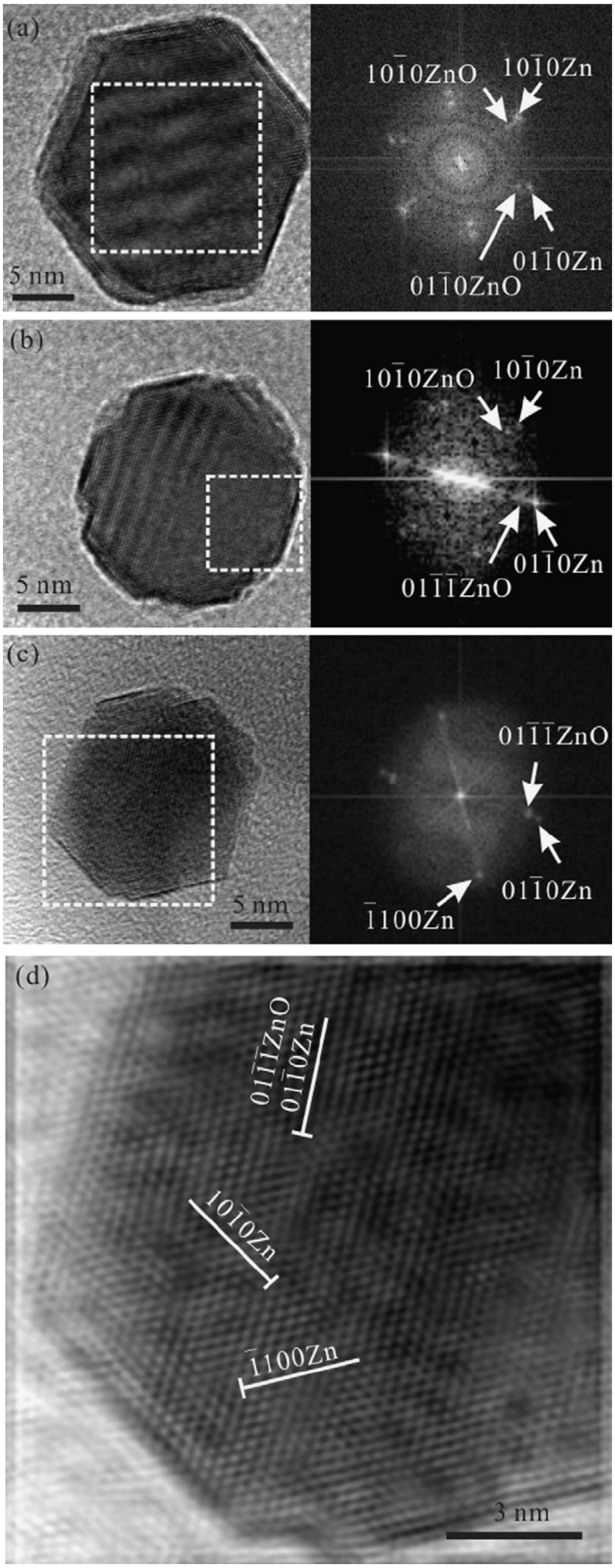

Fig. 5. (a)–(c) Lattice image and corresponding 2D Fourier transform from the square region showing a typical Zn/W-ZnO intergrowth nanocondensate which changed shape, orientation and crystallographic relationship (cf. text) upon electron irradiation for (a) 1 min, (b) 15 min and (c) 30 min. (d) Inverse Fourier transform of the particle in (c) showing fault/slip parallel to $\{1\,0\,\bar{1}\,1\}_{\text{W-ZnO}}$ as well as $(0\,1\,\bar{1}\,0)_{\text{Zn}}$, $(1\,0\,\bar{1}\,0)_{\text{Zn}}$ and $\{\bar{1}\,1\,0\,0\}_{\text{Zn}}$ planes edge-on. The same specimen as Fig. 4.

In addition, the nanosized and (0 0 0 1)-oriented Zn condensates were gradually replaced by $(1\,0\,\bar{1}\,1)$-oriented W-ZnO at a higher oxygen flow rate (cf. Fig. 1). This indicates that oxygen-terminated $(1\,0\,\bar{1}\,1)$ surface of W-ZnO, as mentioned,[3] were favored for some reasons to be clarified in the next section.

High-resolution XRD step-scan coupled with curve fitting by Lorenz distribution (Fig. 1b–d) appeared to have a slightly smaller d-spacing of $(1\,0\,\bar{1}\,1)_{\text{W-ZnO}}$ and $(0\,0\,0\,2)_{\text{Zn}}$ than ambient values (Table 2) despite relatively poor resolution at low 2θ angle. (The d-spacing measurements by high-resolution XRD step-scan are supposed to be accurate within ±0.0001 nm at high 2θ angle.) This may imply a considerable residual stress of the condensates given the third order Birch–Murnaghan equation of state of bulk ZnO with $B_0 = 142.6$ GPa and $B'_0 = 3.6$,[10] and bulk Zn with $B_0 = 58$ GPa and $B'_0 = 6$,[11] although the intimate association of W-ZnO and Zn would make the determination of d-spacings difficult, if not impossible, using either lattice fringes or ring electron diffractions.

The possible residual stress can be attributed to laser ablation process involving extremely rapid heating and cooling as the case of the formation of dense α-PbO_2-type TiO_2 nanocondensates.[12] Alternatively, the residual stress was contributed more from thermal/lattice mismatch of the epitaxial phases when oxygen was introduced in the laser ablation process to form more W-ZnO phase. In this connection, Zn has a higher expansion coefficient ($\alpha = 3 \times 10^{-5}\,\text{K}^{-1}$) than ZnO ($\alpha_a = 4.31 \times 10^{-6}\,\text{K}^{-1}, \alpha_c = 2.49 \times 10^{-6}$).[13] Therefore, thermal mismatch stress due to cooling is expected for the nanocondensates with intimate mixture of Zn and W-ZnO. Under such a circumstance, the residual stress is complicated by lattice mismatch strain given specific crystallographic relationship (Fig. 5).

4.2. *Preferred* $\{1\,0\,\bar{1}\,1\}$ *surfaces for the W-ZnO condensates*

The ZnO condensates have well-developed $\{1\,0\,\bar{1}\,1\}$ surfaces. Apparently, the oxygen-terminated $(0\,\bar{1}\,1\,1)_{\text{W-ZnO}}$ polar surface is relatively inert and well developed than the nonpolar surfaces and the only other polar surface $(0\,0\,0\,1)_{\text{W-ZnO}}$ during dynamic laser ablation condensation in the presence of oxygen. The reasons are threefold. First, $\{0\,\bar{1}\,1\,1\}$ has nearly the

Table 2
Room temperature d-spacings (nm) and Zn/O atomic ratio of co-oriented ZnO $(1\,0\,\bar{1}\,1)$ and Zn (0 0 0 2) nanocondensates in samples prepared under gas flow rate specified in Table 1

Sample	ZnO $(1\,0\,\bar{1}\,1)$[a]	Zn (0 0 0 2)[a]	Zn/O[b]
Vac-0	0.2473	0.2469	4.743
Vac-20	0.2474	0.2467	2.076
Vac-30	0.2476	0.2465	1.411
Ambient standard	0.2476[c]	0.2473[d]	

[a] The observed d-spacings in the XRD pattern of Fig. 1b–d are accurate at best within ±0.0001 nm.
[b] Determined by point-count EDX analysis on the deposit overlaid on glass.
[c] JCPDS file 36-1451.
[d] JCPDS file 04-0831.

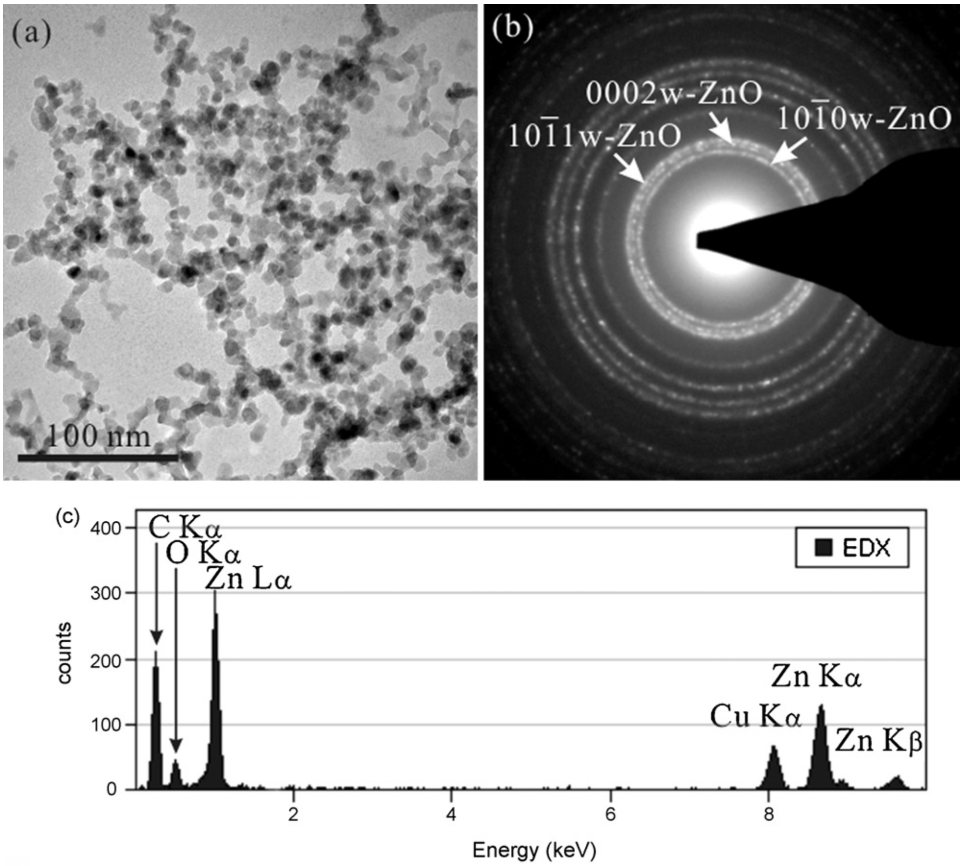

Fig. 6. TEM (a) bright field image and (b) ring SAED pattern of $Zn_{1+x}O$ nanocondensates agglomerated as nanoparticles chain aggregate or in a close packed manner on a carbon-coated collodion film upon pulsed laser ablation at 560 mJ/pulse and oxygen flow rate of 30 mL/min in vacuum. (c) Point-count EDX spectrum of the condensates showing strong Zn and O peaks, with weak C peak from the carbon-coated collodion film and Cu peaks from supporting Cu ring.

same surface density (10.04 atoms/nm^2) as the oxygen close packed (0001) (10.93 atoms/nm^2) in terms of the unrelaxed oxygen surface, and a higher percentage of oxygen occupation than the cation–anion-mixed surfaces such as $(11\bar{2}0)$, $(11\bar{2}1)$ and $(01\bar{1}2)$ (Table 3) given approximate ionic radii of Zn and O.[14] Second (0001) is Zn- or O-terminated, whereas $\{10\bar{1}1\}$ is always O-terminated as mentioned.[3] Third, there are 12 $\{10\bar{1}1\}$ surfaces, i.e. 6 times that of another polar surface (0001). This multiplicity factor is important when total electrostatic energy is of concern.[1]

The $\{10\bar{1}1\}$ surfaces of W-ZnO could also be affected by a deviatoric thermal/lattice mismatch stress during the change from parallel–epitaxial relationship to $[\bar{1}2\bar{1}3]_{\text{W-ZnO}}//[0001]_{\text{Zn}}$; $(01\bar{1}\bar{1})_{\text{W-ZnO}}//(01\bar{1}0)_{\text{Zn}}$. This change involves apparent tilting by $(10\bar{1}0)_{\text{W-ZnO}}$ plane normal for 32° as shown in the stereogram (Fig. 9), in fact fault/slip along $\{01\bar{1}\bar{1}\}_{\text{W-ZnO}}$ and corresponding planes of Zn (Fig. 5d). The $\{01\bar{1}\bar{1}\}_{\text{W-ZnO}}$ slip is consistent with one of the pyramidal slip systems, i.e. $\langle 11\bar{2}0\rangle\{1\bar{1}01\}$ and $\langle 11\bar{2}0\rangle\{1\bar{1}02\}$, operating under an applied stress according to theoretical calculations.[15]

It is of interest to note that $\{10\bar{1}1\}_{\text{W-ZnO}}$ slip was also involved in the electron irradiation-induced rock salt (R) type to W-ZnO transition, following preferential $(1\bar{1}1)_R//(0\bar{1}11)_W$; $[011]_R//[\bar{1}2\bar{1}3]_W$ and then transformation strain induced $(1\bar{1}1)_R//(\bar{1}011)_W$; $[011]_R//[01\bar{1}1]_W$.[16] The two relation-

Table 3
Surface density of ambient W-ZnO with lattice parameters $a = 0.3249$ nm and $c = 0.5206$ nm (JCPDS file 36-1451)

(h k i l)	(0001)	$(10\bar{1}1)$	$(10\bar{1}0)$	$(11\bar{2}0)$	$(11\bar{2}1)$	$(01\bar{1}2)$
Outermost layer (atoms/nm^2)	10.93*	10.04 (O)	12.96	13.36	6.47	7.96
Effective ion occupation (%)	65 (O) 12 (Zn)	60 (O) 11 (Zn)	46	48	23	28

Circular surface area πr^2 for individual ions, i.e. 0.05982 nm^2 and 0.0113 nm^2 given approximate ionic radius (r) 0.138 nm for O and 0.06 nm for Zn[14] were assumed for the calculation of effective ion occupation of the outermost layer. *Notations*: *Either O or Zn; the data without notations are the cases with mixed cations and anions.

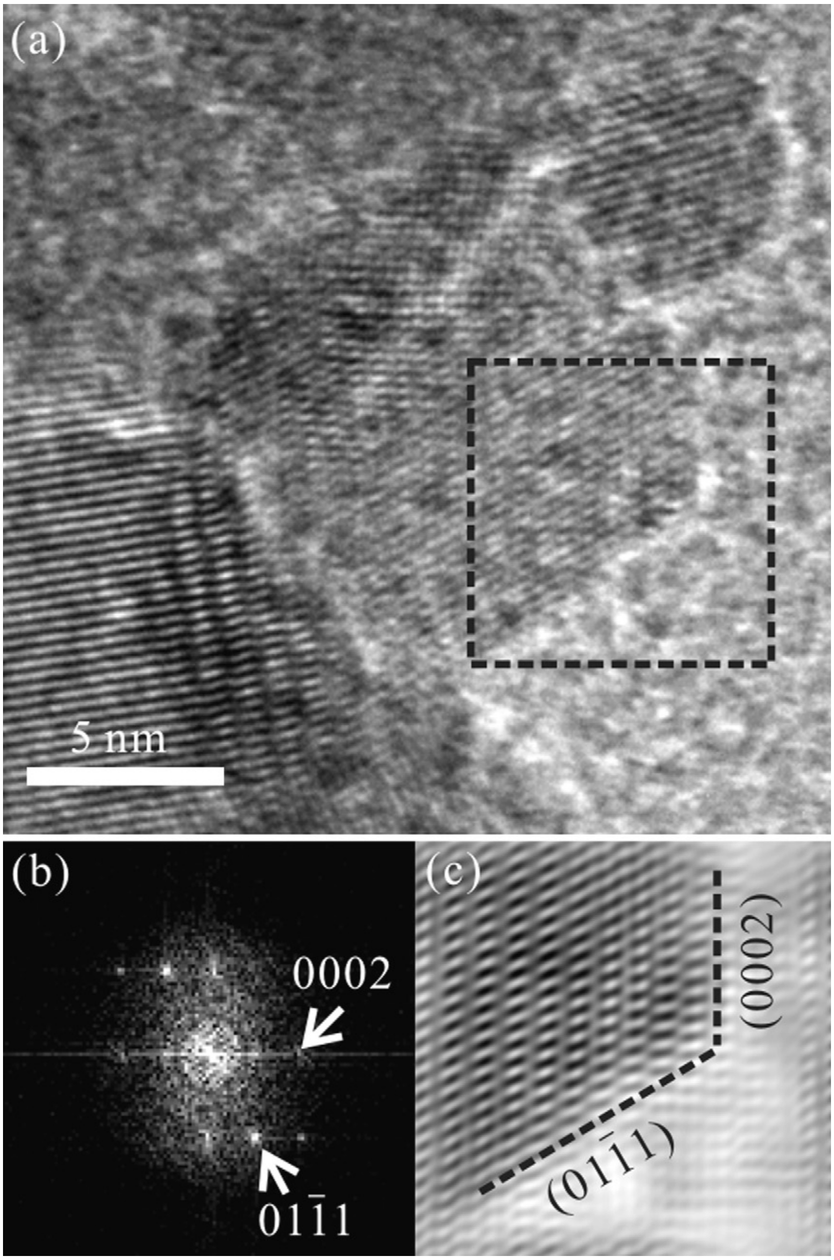

Fig. 7. Lattice image of the $Zn_{1+x}O$ nanocondensates. (b) and (c) Forward and inverse Fourier transform from the square region in (a), showing a condensate in $[0\,\bar{1}\,1\,0]$ zone axis with well-developed $(0\,\bar{1}\,1\,1)$ and $\{0\,0\,0\,1\}$ polar surfaces. The same specimen as Fig. 6.

ships can be rationalized by specified extent of chair- and boat-type Peierls distortions accompanied with band gap opening and intermediate $\{1\,1\,1\}_R$ slip for energetically favorable $\{1\,1\,1\}_R//(0\,1\,\bar{1}\,1)_W$ match.[16] Thus, it cannot be excluded that the $\{1\,0\,\bar{1}\,1\}$ surfaces of W-ZnO were derived from $\{1\,1\,1\}$ of the rock salt-type nuclei.

Finally, the Zn condensates have well-developed $\{1\,0\,\bar{1}\,0\}$, $\{1\,0\,\bar{1}\,1\}$ and $\{0\,0\,0\,1\}$ faces according to the present observations and previous suggestion for the Zn particles prepared by an alternative method of pulsed CO_2 laser melting of Zn target in vacuum.[17] The W-ZnO condensate of well-developed $\{1\,0\,\bar{1}\,1\}$ polar surfaces is hardly a pseudomorph of parallel–epitaxial Zn condensate, otherwise the alternative polar surface, i.e. $(0\,0\,0\,1)$, would be favored. On the other hand, the $\{1\,0\,\bar{1}\,1\}$ polar surfaces could partly be derived from $(0\,1\,\bar{1}\,0)_{Zn}$ of the Zn condensates when the relationship $[\bar{1}\,2\,\bar{1}\,3]_{W\text{-}ZnO}//[0\,0\,0\,1]_{Zn}$; $(0\,1\,\bar{1}\,\bar{1})_{W\text{-}ZnO}//(0\,1\,\bar{1}\,0)_{Zn}$ (Fig. 9b) was followed.

4.3. Artificial epitaxy

Having well-developed surface of $\{1\,0\,\bar{1}\,1\}$ for W-ZnO, the condensates tended to coalesce and rest with such habit planes when deposited on an amorphous substrate. Such an artificial epitaxy depends on the shape of the crystallites in assembly, as the cases of laser ablation deposition of CeO_2,[18] more or less facilitated by $\{1\,1\,1\}$-specific coalescence twins[19] and

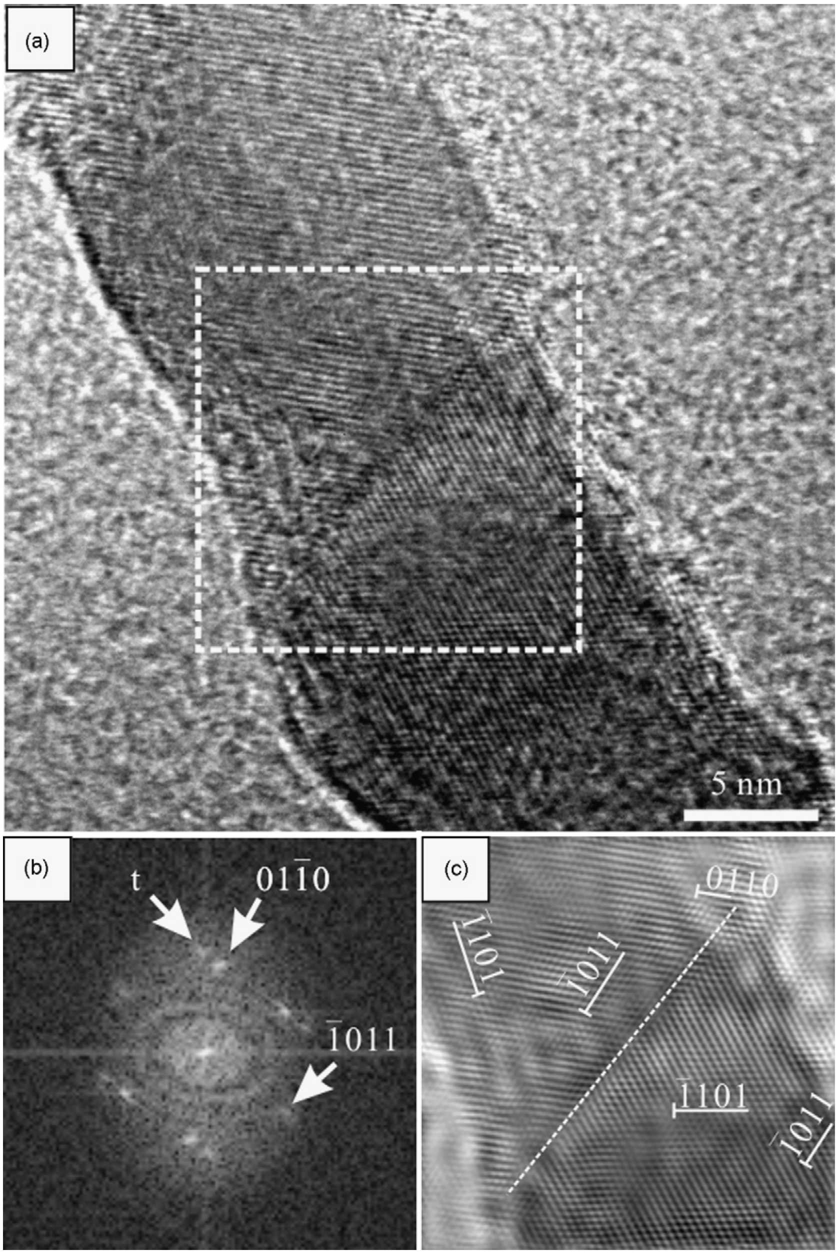

Fig. 8. (a) Lattice image of twinned ZnO nanocondensates prepared by additional pulsed laser ablation at 1040 mJ/pulse under free run in air. (b) and (c) two-dimensional forward and inverse Fourier transform from the square region in (a) showing the bicrystals have $(\bar{1}\,1\,0\,1)$ twin boundary and twin spot (denoted as t) in $[2\,\bar{1}\,\bar{1}\,3]$ zone axis with dislocation half plane parallel to $(\bar{1}\,1\,0\,1)$ $(0\,1\,\bar{1}\,0)$ and $(\bar{1}\,0\,1\,1)$ polar surfaces.

CeO$_{2-x}$ epitaxial domains on glass,[20] rather than surface relief of the substrate.[6] The $\{1\,0\,\bar{1}\,1\}$-specific coalescence of W-ZnO to form twin and single crystal was indeed observed in the present study, although it is not clear whether or not the oxygen-terminated $\{1\,0\,\bar{1}\,1\}$ surface has opposite polarity for impingement.

Thermally activated Brownian rotation-coalescence of the crystallites over a substrate[21–25] and within a film of considerable thickness[26] may cause preferred orientation of the assembled condensates. Given nanometer size and radiant heating effect of pulse laser ablation deposition, the Brownian-type rotation-coalescence of the Zn/W-ZnO condensates is expected to proceed not only over the substrate but also in the film of a considerable thickness without a preheating treatment. In this connection, crystalline TiO$_2$[27] and Al$_2$O$_3$[28] nanocondensates via pulse laser ablation deposition were also known to form NCA or in a closer packed manner on a supporting film without a preheating treatment yet with a considerable effect of gray body radiation heating. (Temperature up to ca. 1000 °C was suggested for the nanocondensates to assemble as a close packed manner via such a dynamic process.[12,27]) Besides, the preferred orientation of TiC coating on steel substrate[26] and CeO$_2$ coating on Si or glass[18] was found to change with deposition time, indicating the Brownian-type

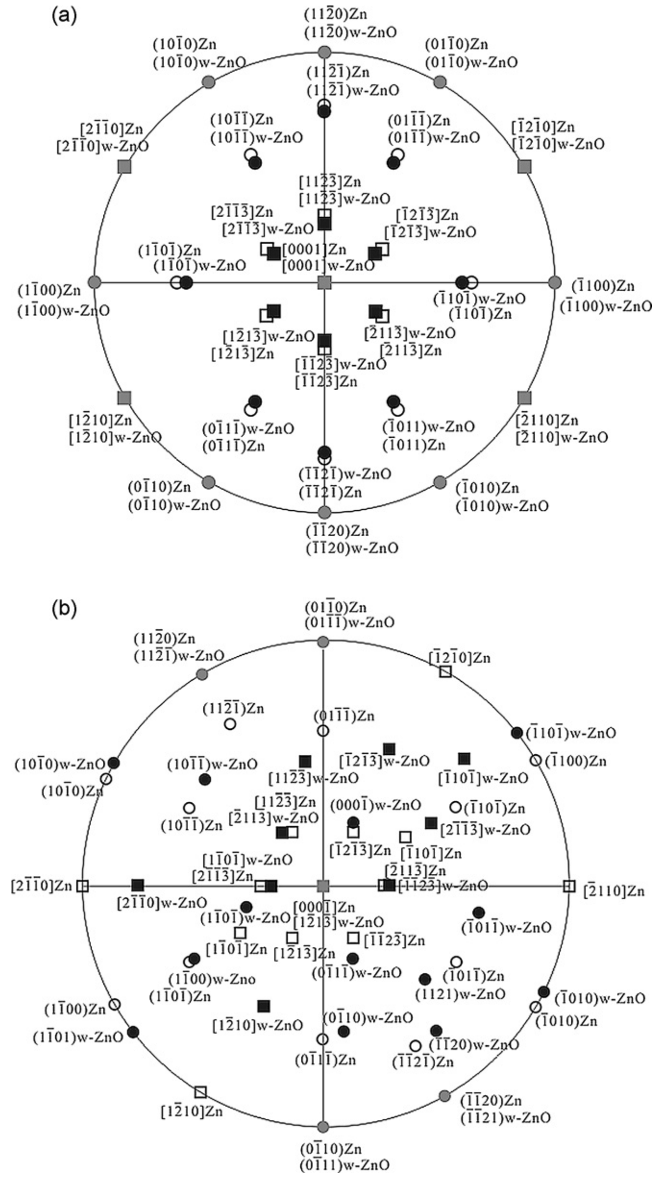

Fig. 9. Stereographic projection of the epitaxial relationships: (a) $[0\,0\,0\,1]_{\text{W-ZnO}}//[0\,0\,0\,1]_{\text{Zn}}$; $(1\,0\,\bar{1}\,0)_{\text{W-ZnO}}//(1\,0\,\bar{1}\,0)_{\text{Zn}}$ and (b) $[\bar{1}\,2\,\bar{1}\,3]_{\text{W-ZnO}}//[0\,0\,0\,1]_{\text{Zn}}$; $(0\,1\,\bar{1}\,\bar{1})_{\text{W-ZnO}}//(0\,1\,\bar{1}\,0)_{\text{Zn}}$, as observed in Fig. 5a and b, respectively. Squares denote zone axes; whereas open, dark and gray circles denote plane normals for Zn, W-ZnO, and superimposed Zn/W-ZnO, respectively.

rotation-coalescence process indeed occurred for the deposited particles.

5. Conclusions

Pulse laser ablation on Zn target in the presence of oxygen was shown to cause unusual preferred orientation $\{1\,0\,\bar{1}\,1\}$ for the W-ZnO condensates with considerable residual stress when deposited on a glass substrate. This type of artificial epitaxy on glass is due to a unique shape of the W-ZnO condensates, i.e. well-developed polar surfaces $\{1\,0\,\bar{1}\,1\}$ rather than $(0\,0\,0\,1)$ for coalescence as unity or twin. This knowledge is of importance to the understanding of preferred orientation of W-ZnO on semiconductors with polycrystalline or amorphous buffer layers. The W-ZnO condensates with predominant surfaces $\{1\,0\,\bar{1}\,1\}$ could be used for self-catalyzed vapor–liquid–solid growth of rod-like W-ZnO whiskers with unusual habit, i.e. extending along the zone axes of the well-developed polar surfaces $\{1\,0\,\bar{1}\,1\}$,[7] for potential semiconducting, piezoelectric and/or catalytic applications because of directional dependence of physical/chemical properties.

Acknowledgements

We thank C.N. Huang for the help on laser ablation process, L.J. Wang for technical assistance on TEM. Supported by Center for Nanoscience and Nanotechnology at NSYSU and National Science Council, Taiwan, ROC under contract NSC96-2221-E214-037.

References

1. Wang, Z. L., Kong, X. Y., Ding, Y., Gao, P., Hughes, W. L., Yang, R. and Zhang, Y., Semiconducting and piezoelectric oxide nanostructures induced by polar surfaces. *Adv. Funct. Mater.*, 2004, **14**, 943–956.
2. Yang, R., Ding, Y. and Wang, Z. L., Deformation-free single-crystal nanohelixes of polar nanowires. *Nano Lett.*, 2004, **4**, 1309–1312.
3. Ding, Y. and Wang, Z. L., Profile imaging of reconstructed polar and non-polar surfaces of ZnO. *Surf. Sci.*, 2007, **601**, 425–433.
4. Huang, M. H., Wu, Y., Feick, H., Tran, N., Weber, E. and Yang, P., Catalytic growth of zinc oxide nanowires by vapor transport. *Adv. Mater.*, 2001, **13**, 113–116.
5. Ding, Y., Gao, P. X. and Wang, Z. L., Catalyst–nanostructure interface lattice mismatch in determining the shape of VLS grown nanowires and nanobelts: a case of Sn/ZnO. *J. Am Chem. Soc.*, 2004, **126**, 2066–2072.
6. Givargizov, E. I., *Oriented Crystallization on Amorphous Substrates*. Plenum Press, New York, 1991.
7. Huang, B. H., Chen, S. Y. and Shen, P., $\{1\,0\,\bar{1}\,1\}$ and $\{1\,1\,\bar{2}\,1\}$-specific growth and twinning of ZnO whiskers. *J. Phys. Chem. C*, 2008, **112**, 1064–1071.
8. Williams, D. B., *Practical Analytical Electron Microscopy in Materials Science*. Philips Electronic Instruments Inc., Mahwah, 1984.
9. Winchell, A. N. and Winchell, H., *Elements of Optical Mineralogy—An Introduction to Microscopic Petrography* (*4th edition*). Wiley, New York, 1961, p. 59.
10. Desgreniers, S., Structural and compressive high-density phases of ZnO: parameters. *Phys. Rev. B*, 1998, **58**, 14102–14105.
11. Takemura, K., Zn under pressure: a singularity in the hcp structure at *c*/*a* = *sqrt*[3]. *Phys. Rev. Lett.*, 1995, **75**, 1807–1810.
12. Chen, S. Y. and Shen, P., Laser ablation condensation of α-PbO$_2$-type TiO$_2$. *Phys. Rev. Lett.*, 2002, **89**, 096106-1–096106-4.
13. Coleman, V. A. and Jagadish, C., Basic properties and applications of ZnO. In *Zinc Oxide Bulk, Thin Films and Nanostructures*, ed. C. Jagadish and S. J. Pearton. Elsevier, Oxford, 2006, p. 12.
14. Shannon, R. D., Revised effective ionic radii and systematic studies of interatomic distances in halides and chalcogenides. *Acta Crystallogr. A*, 1976, **32**, 751–767.
15. Shintani, K., Line tension and configuration of a dislocation on the basal, prismatic, and pyramidal planes in zinc oxide. *Phys. Rev. B*, 1993, **47**, 7032–7035.
16. Chen, S. Y., Shen, P. and Jiang, J., Polymorphic transformation of dense ZnO nanoparticles: implications for chair/boat-type Peierls distortions of AB semiconductor. *J. Chem. Phys.*, 2004, **121**, 11309–11313.
17. Wu, R., Xie, C., Hu, J., Xia, H. and Wang, A., Function of oxide film during the thermal oxidation process of Zn nanoparticles. *Scripta Mater.*, 2000, **43**, 841–846.
18. Kuo, L. Y. and Shen, P., Shape and preferred orientation of CeO$_2$ condensates. *Mater. Sci. Eng. A*, 2000, **277**, 258–265.

19. Lee, W. H. and Shen, P., On the coalescence and twinning of cubo-octahedral CeO_2 condensates. *J. Cryst. Growth*, 1999, **205**, 169–176.
20. Lee, W. H. and Shen, P., Laser ablation deposition of CeO_{2-x} epitaxial domains on glass. *J. Solid State Chem.*, 2002, **166**, 197–202.
21. Masson, A., Métois, J. J. and Kern, R., Migration brownienne de cristallites sur une surface et relation avec l'épitaxie I. partie expérimentale. *Surf. Sci.*, 1971, **27**, 463–482.
22. Métois, J. J., Gauch, M., Masson, A. and Kern, R., Migration brownienne de cristallites sur une surface et relation avec l'épitaxie III cas de l'aluminium sur KCl: précisions sur le méchanisme de glissement. *Surf. Sci.*, 1972, **30**, 43–52.
23. Métois, J. J., Migration brownienne de cristallites sur une surface et relation avec l'épitaxie IV. mobilité de cristallites sur une surface: décoration de gradins monoatomiques de surface. *Surf. Sci.*, 1973, **36**, 269–280.
24. Kern, R., Masson, A. and Métois, J. J., Migration brownienne de cristallites sur une surface et relation avec l'épitaxie II. partie théorique. *Surf. Sci.*, 1971, **27**, 483–498.
25. Kuo, L. Y. and Shen, P., On the rotation of nonepitaxy crystallites on single crystal substrate. *Surf. Sci.*, 1997, **373**, L350–L356.
26. Kuo, L. Y. and Shen, P., On the condensation and preferred orientation of TiC nanocrystals—effects of electric field, substrate temperature and second phases. *Mater. Sci. Eng. A*, 2000, **276**, 99–107.
27. Tsai, M. H., Chen, S. Y. and Shen, P., Laser ablation condensation of TiO_2 particles: effects of laser energy, oxygen flow rate and phase transformation. *J. Aerosol Sci.*, 2005, **36**, 13–25.
28. Pan, C., Chen, S. Y. and Shen, P., Laser ablation condensation, coalescence and phase change of dense γ-Al_2O_3 particles. *J. Phys. Chem. B*, 2006, **110**, 24340–24345.